Investigation of the spin-1 honeycomb antiferromagnet BaNi₂V₂O₈ with easy-plane anisotropy

E. S. Klyushina, ^{1,2,*} B. Lake, ^{1,2} A. T. M. N. Islam, ¹ J. T. Park, ³ A. Schneidewind, ⁴ T. Guidi, ⁵ E. A. Goremychkin, ⁵ B. Klemke, ¹ and M. Månsson ^{6,7}

¹Helmholtz-Zentrum Berlin für Materialien und Energie, 14109 Berlin, Germany
²Institut für Festkörperphysik, Technische Universität Berlin, 10623 Berlin, Germany
³Heinz Maier-Leibnitz Zentrum, TU München, D-85747 Garching, Germany
⁴Forschungszentrum Jülich GmbH, Jülich Centre for Neutron Science at MLZ, Lichtenbergstr. 1, D-85747 Garching, Germany
⁵ISIS Facility, Rutherford Appleton Laboratory, Chilton, Didcot, Oxon OX11 0QX, United Kingdom
⁶Materials Physics, KTH Royal Institute of Technology, SE-16440 Stockholm Kista, Sweden
⁷Laboratory for Neutron Scattering & Imaging, Paul Scherrer Institute, CH-5232 Villigen, Switzerland
(Received 11 September 2017; revised manuscript received 13 November 2017; published 21 December 2017)

The magnetic properties of the two-dimensional, S=1 honeycomb antiferromagnet BaNi₂V₂O₈ have been comprehensively studied using dc susceptibility measurements and inelastic neutron scattering techniques. The magnetic excitation spectrum is found to be dispersionless within experimental resolution between the honeycomb layers, while it disperses strongly within the honeycomb plane where it consists of two gapped spin-wave modes. The magnetic excitations are compared to linear spin-wave theory allowing the Hamiltonian to be determined. The first- and second-neighbor magnetic exchange interactions are antiferromagnetic and lie within the ranges $10.90 \text{ meV} \leqslant J_n \leqslant 13.35 \text{ meV}$ and $0.85 \text{ meV} \leqslant J_{nn} \leqslant 1.65 \text{ meV}$, respectively. The interplane coupling J_{out} is four orders of magnitude weaker than the intraplane interactions, confirming the highly two-dimensional magnetic behavior of this compound. The sizes of the energy gaps are used to extract the magnetic anisotropies and reveal substantial easy-plane anisotropy and a very weak in-plane easy-axis anisotropy. Together these results reveal that BaNi₂V₂O₈ is a candidate compound for the investigation of vortex excitations and Berezinsky-Kosterliz-Thouless phenomenon.

DOI: 10.1103/PhysRevB.96.214428

I. INTRODUCTION

It is possible to realize low-dimensional magnetic systems in real three-dimensional (3D) crystal structures. This is because in some cases the exchange interactions between magnetic ions exist only along particular directions within the crystal lattice due to their strong dependence on the overlap of electronic orbitals. Thus, the properties of low-dimensional magnetic systems can be investigated experimentally allowing the intriguing phenomena predicted for these Hamiltonians to be tested. While physical realizations of numerous low-dimensional magnetic models such as one-dimensional (1D) spin- $\frac{1}{2}$ antiferromagnetic chains [1], Haldane chains [2], and spin ladders [3] are already discovered and well explored, there are still models whose solid-state prototypes are very rare or as yet undiscovered. A remarkable example is the two-dimensional (2D) Heisenberg magnet with easy-plane anisotropy which has attracted attention as a candidate to display Berezinsky-Kosterliz-Thouless (BKT) phenomenon [4–7].

Although the existence of conventional long-range magnetic order at finite temperatures is prohibited by the Merim-Wagner theorem [8] for 2D XY magnetic systems, a topological phase transition from a disordered to a quasi-long-range magnetically ordered state has been theoretically proposed. Kosterliz and Thouless [6,7] independently with Berezinsky [4,5] suggested the presence of topological defects known as spin-vortices characterized by a topological winding number in

2D XY magnetic systems at finite temperatures. These vortices couple into vortex/antivortex pairs below the finite transition temperature $T_{\rm BKT}$ resulting in a quasi-long-range magnetically ordered state.

So far, the BKT transition was experimentally observed only in superfluids [9] and superconducting thin films [10,11] which are good physical realizations of 2D XY models, or under applied magnetic field in Cu-based dimerized coordination polymers [12]. However, quantum Monte Carlo simulations [13,14] predict that the BKT transition can also be observed in 2D Heisenberg magnetic systems which have only weak easy-plane (XXZ-type) anisotropy spurring interest to search for and investigate magnetic compounds which are physical realization of the 2D XXZ Heisenberg model.

Layered honeycomb antiferromagnets are promising candidates to realize 2D magnetic systems. Some indications of the free vortex phase have been found in the honeycomb antiferromagnet MnPS₃ where the temperature dependence of the magnetic correlation length revealed the predicted BKT exponential dependence rather than the usual power-law dependence of conventional magnets [15,16]. However, the BKT transition is obscured in this compound by the onset of long-range magnetic order which occurs at a higher temperature.

Two other well-explored honeycomb antiferromagnets are $BaNi_2(AsO_4)_2$ and $BaNi_2(PO_4)_2$ where the magnetic Ni^{2+} ions have spin-1 (S=1) and also develop conventional longrange antiferromagnetically ordered ground states with easy-plane anisotropy [17–19]. The interplane magnetic exchange coupling in both compounds is extremely weak and was found to be three orders of magnitude weaker than the dominant intraplane magnetic exchange interaction. The heat

^{*}Corresponding author: ekaterina.klyushina@helmholtz-berlin.de

capacity [17], however, revealed the behavior typical of a 3D Heisenberg magnetic system with a characteristic sharp λ peak at a finite ordering temperature T_N , rather than the broad maximum and smooth features expected for the heat capacity of a 2D magnetic system [20].

The compound $BaNi_2V_2O_8$ belongs to the same class of Nibased layered honeycomb antiferromagnets as $BaNi_2(AsO_4)_2$ and $BaNi_2(PO_4)_2$, but has been much less explored. The crystal structure of $BaNi_2V_2O_8$ has space group $R\bar{3}$ with lattice constants $a=b=5.0375\,\text{Å}$ and $c=22.33\,\text{Å}$. The S=1 magnetic Ni^{2+} ions are surrounded by O^{2-} ions forming edge-sharing NiO_6 octahedra which are arranged into honeycomb layers within the ab plane. These layers are well separated along the c axis by Ba^{2+} ions and nonmagnetic $V^{5+}O_4$ tetrahedra. The distance between the layers is three times larger than the distance between the nearest-neighbor magnetic ions within the plane suggesting that the interactions between the honeycomb layers are weak.

Powder neutron diffraction measurements reveal that the spins develop long-range magnetic order below the transition temperature $T_N \sim 50$ K [21]. In contrast, the reported dc magnetic susceptibility and heat-capacity data display no clear signatures of the transition to the ordered state and suggest predominantly two-dimensional behavior. In particular, the heat-capacity data [22] are in good agreement with the theoretical predictions of quantum Monte Carlo simulations performed for quasi-2D Heisenberg systems [20] confirming the predominantly 2D character of BaNi₂V₂O₈. The presence of easy-plane anisotropy is revealed by the susceptibility data that show a strong difference between the measurements with magnetic field applied in plane and out of plane which persists to temperatures well above T_N [21].

The magnetic structure of BaNi₂V₂O₈ was solved by Rogato et. al. [21]. In the ground state the spins lie within the honeycomb plane and are collinear so that each spin is antiparallel to its three nearest neighbors (red arrows in Fig. 1). This magnetic structure suggests that the dominant exchange interaction is antiferromagnetic between firstnearest-neighbor Ni²⁺ ions [beige solid lines in Fig. 1(a)]. Its strength was estimated to be $J_n = 8.27$ meV from susceptibility measurements [21] (all magnetic exchange constants are stated assuming single counting of each magnetic bond and where a positive sign defines an AFM interaction). Second-neighbor interactions J_{nn} [dotted magenta lines in Fig. 1(a)] and third-neighbor interactions J_{nnn} [dashed-dotted green lines in Fig. 1(a)] may also be present. Figure 1(b) shows the possible magnetic exchange paths responsible for the interplane coupling. J_{out1} (dashed-dotted orange lines) and J_{out2} (dotted green lines) correspond to the shortest and next-shortest distances between parallel and antiparallel spins in neighboring honeycomb planes, respectively, and the path J_{out3} is realized via the shortest distance between antiparallel spins in the first and third honeycomb layers. Altogether, the available results for BaNi₂V₂O₈ imply that this compound is a quasi-2D Heisenberg antiferromagnet with easy-plane anisotropy and suggests it is suitable for investigations of BKT phenomena. Indeed, recent ⁵¹V nuclear magnetic resonance [23] and electronic spin resonance [24] measurements reveal that the correlation length of BaNi₂V₂O₈ decays exponentially

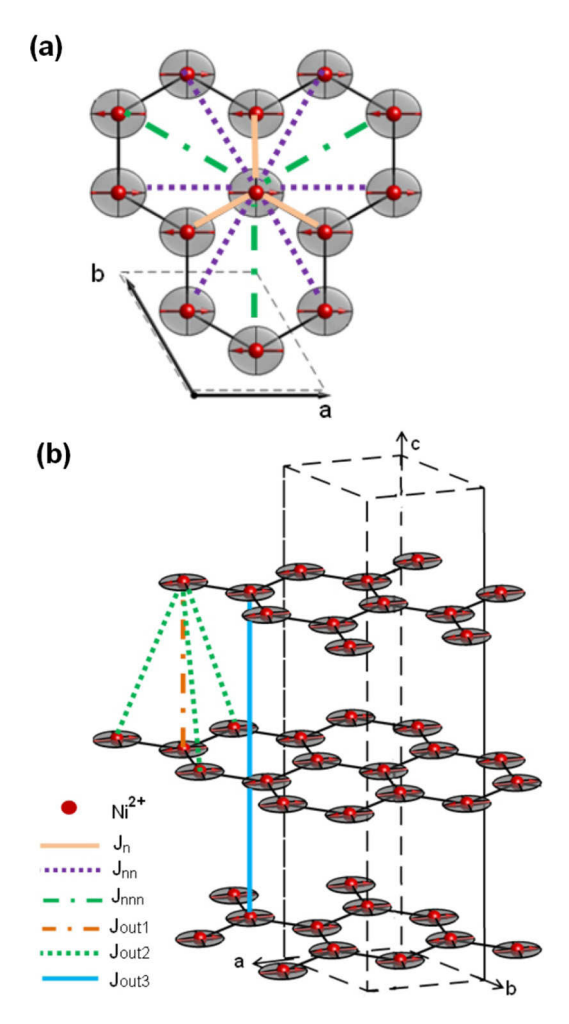


FIG. 1. Crystal and magnetic structure (one twin) of $BaNi_2V_2O_8$ within (a) a honeycomb plane and (b) a single unit cell. Only the magnetic Ni^{2+} ions are shown for clarity. The magnetic structure is based on the results of powder neutron diffraction measurements [21]. The red arrows represent spin directions and the gray ellipsoids illustrate the easy-plane single-ion anisotropy. The magnetic exchange interactions are represented by the colored lines and are discussed in Sec. III C.

as a function of temperature in agreement with the Berezinsky-Kosterlitz-Thouless theory [7].

Despite these promising results, the Hamiltonian of $BaNi_2V_2O_8$ is currently unknown. In this paper, the magnetic properties of this compound are explored using dc susceptibility measurements along with powder and single-crystal inelastic neutron scattering (INS) measurements. The dc susceptibility measurements are performed up to high temperatures (2 K $\leq T \leq$ 640 K) which allow the total value of the magnetic exchange interactions J_{total} to be determined. The single-crystal INS measurements at base temperature reveal spin-wave excitations which disperse within the honeycomb plane and are completely dispersionless in the out-of-plane direction confirming the strongly 2D magnetic behavior of $BaNi_2V_2O_8$. The magnetic excitation spectrum consists of two modes which are both gapped, suggesting a dominant easy-plane anisotropy and a weak easy-axis anisotropy which

gives the preferred directions within this plane. The magnetic excitations are analyzed using linear spin-wave theory which allows the exchange interactions and anisotropies to be extracted. The Hamiltonian of BaNi₂V₂O₈ is solved and found to be closer to an ideal 2D antiferromagnet with easy-plane anisotropy than BaNi₂(AsO₄)₂ and BaNi₂(PO₄)₂. Thus, this compound is a promising candidate to display BKT phenomena above T_N where the system is in a quasi-2D XY regime. According to the BKT theory [6,7], this behavior manifests itself as an exponential decay of the order parameter above the transition temperature $T_{\rm BKT}$.

II. EXPERIMENTAL DETAILS

Powder and single-crystalline samples of $BaNi_2V_2O_8$ were grown in the Core Lab for Quantum Materials at the Helmholtz Zentrum Berlin für Materialien und Energie (HZB) in Germany. The single-crystal growth was performed in a four-mirror optical image furnace using the traveling-solvent-floating-zone method. Feed rods for the growth were prepared by solid-state reaction of high-purity powders of $BaCO_3$, NiO_3 , and V_2O_5 in air. A solvent with excess BaV_2O_6 was attached to the tip of the feed rod as a flux compound to facilitate the growth at a lower temperature. The growth was performed at a rate of $0.2 \ mm/h$ in air atmosphere.

Single-crystal static magnetic susceptibility measurements were performed on BaNi₂V₂O₈ at the Core Lab for Quantum Materials, HZB, using a Physical Property Measurement System (PPMS) and a Magnetic Property Measurement System with a Vibrating Sample Magnetometer (MPMS-VSM) by Quantum Design. Three single-crystal samples with masses of 8.48, 19.38, and 4.85 mg were cut from different single-crystal growths and data were collected under a magnetic field of 1 T applied both parallel and perpendicular to the c axis. The measurements were performed at both low (2–400 K) and high (300–640 K using a heater stick) temperatures. The upper temperature was limited to be below the temperature of 650 K at which the sample undergoes structural changes. The data collected in the low- and high-temperature regimes were combined by averaging over the overlapping temperature range (300-400 K).

Both powder and single-crystal inelastic neutron scattering (INS) measurements were performed to explore the magnetic excitation spectrum of BaNi₂V₂O₈. Powder INS data were collected using a new high count rate thermal time-of-flight spectrometer MERLIN [25] at ISIS, Rutherford Appleton Laboratory, U. K. The polycrystalline sample with total mass of 19.03 g was cooled to the base temperature of 5 K using a closed cycle refrigerator. The Fermi chopper was operated in four different modes phased to give incident neutron energies of $E_i = 80, 50, 35$ and 20 meV, respectively. For these energies the chopper frequencies were 400, 300, 250, and 200 Hz and the corresponding resolutions at the elastic energy were $E_i = 5.1 \pm 0.1$, 3.2 ± 0.06 , 2.26 ± 0.06 , and 1.24 ± 0.02 meV, respectively. These resolution values were extracted by fitting the incoherent elastic signal. A vanadium standard was used to normalize the detectors.

Single-crystal INS measurements were performed on the thermal neutron triple-axis spectrometer PUMA [26] at the Heinz Maier-Leibnitz Zentrum (MLZ), Garching, Germany.

The single-crystal sample of $BaNi_2V_2O_8$ with mass of 340 mg was preoriented with the (h,k,0) plane as the horizontal instrumental scattering plane and was cooled to the base temperature of 3.5 K by a closed-cycle cryostat. The instrument was equipped with a double-focused pyrolytic graphite [PG(002)] monochromator and analyzer operated at the fixed final wave vector of $k_f = 2.662 \text{ Å}^{-1}$ giving an elastic energy resolution of 0.8 meV. A sapphire filter was located before the monochromator to reduce the fast neutron background while two PG filters were placed in series between the sample and analyzer to eliminate higher-order neutrons from the scattered beam.

For a detailed investigation of the low-energy excitation spectra, the same sample was measured on the cold neutron triple-axis spectrometer PANDA [27] at the Heinz Maier-Leibnitz Zentrum (MLZ), Garching, Germany. PANDA was equipped with a double-focusing PG(002) monochromator and analyzer. The measurements were performed in both the (h,k,0) and (h,0,l) scattering planes at the base temperature of 4.3 K, which was achieved by using a closed-cycle cryostat. All data were collected at the fixed final wave vector $k_f = 1.57 \text{ Å}^{-1}$ and the elastic energy resolution was 0.1379 meV. A beryllium filter was used to remove the high-order wavelengths diffracted by the monochromator.

A larger single crystal of $BaNi_2V_2O_8$ with mass of 500 mg was measured using the cold-neutron triple-axis spectrometer TASP [28], at the Paul Scherrer Institute (PSI), Switzerland. The sample was preoriented with (h,k,0) plane as the instrumental scattering plane and was cooled down to 1.47 K using an orange cryostat.

The measurements were carried out in the (h,k,0) and (h,k,h/2) scattering planes where (h,k,h/2) was achieved by tilting (h,k,0) by 5° about the horizontal axis perpendicular to the (0,1,0) direction. This instrument was equipped with a vertically focused PG(002) monochromator and a horizontally focused PG(002) analyzer. The final wave vector was fixed at $k_f = 1.23 \text{ Å}^{-1}$ giving an energy resolution of 0.065 meV.

To further explore the magnetic excitation spectra of BaNi₂V₂O₈ along all reciprocal space directions including off-symmetry directions, the single-crystalline sample of BaNi₂V₂O₈ with mass of 500 mg was measured using the cold-neutron multichopper spectrometer LET [29] at ISIS, Rutherford Appleton Laboratory, U. K. This spectrometer uses the time-of-flight technique which allows a large region of reciprocal space (several Brillouin zones) and a wide range of energy transfers to be measured simultaneously. The orientation of the sample was aligned with the (h,k,0) plane as the horizontal instrument scattering plane and cooled down to T = 5 K using a closed-cycle refrigerator. The INS data were collected at four different incident energies of $E_i = 2.97, 5,$ 10.2, and 30 meV simultaneously which are characterized by calculated elastic energy resolutions of $\Delta E_i = 0.05, 0.1, 0.31,$ and 1.2 meV, respectively.

The powder and single-crystal magnetic excitation spectra of $BaNi_2V_2O_8$ were analyzed using the SPINW MATLAB Library [30] which can perform numerical calculations of the spin-wave energies and intensities for complex magnetic lattices with commensurate or incommensurate magnetic order.

III. RESULTS AND ANALYSIS

A. Static susceptibility

Figure 2(a) shows the single-crystal dc magnetic susceptibility data collected on the single-crystalline samples of BaNi₂V₂O₈ over the temperature range 2 K to 640 K under a dc magnetic field of 1 T applied parallel ($\chi_{H\parallel c}$) and perpendicular ($\chi_{H\perp c}$) to the c axis. The data were collected on different single-crystalline samples to improve the statistics and to check for consistency.

Both $\chi_{H\parallel c}$ and $\chi_{H\perp c}$ display a broad maximum in the vicinity of $T\approx 150~{\rm K}$ which indicates the presence of short-range magnetic correlations. Above this maximum, the susceptibilities show the same behavior and smoothly decrease with increasing temperature, suggesting that the magnetism is isotropic. A small difference between the magnitude of $\chi_{H\parallel c}$ and $\chi_{H\perp c}$ observed at high temperatures can be attributed to the anisotropy of the Landé g factor which has the values $g_{H\perp c}=2.243$ and $g_{H\parallel c}=2.225$ [23].

Below the maximum, the susceptibility starts to display anisotropic behavior which first appears at $T_{\rm ani}=80~{\rm K}$ below which $\chi_{H\parallel c}$ and $\chi_{H\perp c}$ split from each other. The anisotropy becomes more pronounced as temperature decreases. Indeed, below $80~{\rm K},~\chi_{\perp c}$ continuously decreases, in contrast to $\chi_{H\parallel c}$ which shows a weak minimum at $T_{\rm XY}=52~{\rm K}$ and then increases slightly and becomes constant with further temperature decrease.

1. Low-temperature susceptibility

Figure 2(b) shows the first derivative of $\chi_{H\parallel c}$ and $\chi_{H\perp c}$ with respect to temperature plotted over the temperature range from

2 K to 200 K. This plot reveals that at T=52 K $\frac{d\chi_{H\parallel c}}{dT}=0$, satisfying the condition for an extremum and confirming that $\chi_{H\parallel c}$ has a minimum at this temperature. The first derivative of $\chi_{H\perp c}$ with respect to temperature has a sharp maximum at T=52 K which means that second derivative satisfies the condition for an inflection point $(\frac{d^2\chi_{H\perp c}}{dT^2}=0)$ at this temperature.

These results can be compared with the predictions of quantum Monte Carlo (QMC) simulations performed by Cuccoli *et al.* [13,14] for the 2D, spin- $\frac{1}{2}$ square lattice with Ising (XXZ-type) interactions. According to these simulations, the in-plane susceptibility decreases continuously with decreasing temperature [13,14]. In contrast, the out-of-plane susceptibility has a minimum at a finite temperature T_{co} which was assigned by Cuccoli *et al.* [13,14] to the transition to a regime where the spins lie predominantly in the XY plane. Thus, the minimum observed in the $\chi_{H\parallel c}$ data of BaNi₂V₂O₈ at $T_{\rm XY} = 52$ K could be a signature of a crossover to a regime dominated by easy-plane anisotropy.

Indeed, the behavior observed in $\chi_{H\parallel c}$ and $\chi_{H\perp c}$ in BaNi₂V₂O₈ below $T_{\rm XY}=52$ K is consistent with the behavior expected for $\chi_{H\parallel c}$ and $\chi_{H\perp c}$ of a conventional AFM below its Néel temperature T_N (when the spins are ordered within the plane perpendicular to the c axis). However, the temperature $T_{\rm XY}=52$ K is higher than $T_N=50$ K proposed in the literature for BaNi₂V₂O₈ [21]. Neither $\chi_{H\parallel c}$ nor $\chi_{H\perp c}$ reveal clear signatures for the phase transition to the magnetically ordered state proposed at ≈ 50 K by powder neutron diffraction measurements [21].

Indeed, only the first derivative of the $\chi_{H\parallel c}$ has a sharp minimum at 48 K \pm 0.5 K satisfying the condition $\frac{d^2\chi_{H\parallel c}}{dT^2}=0$ for

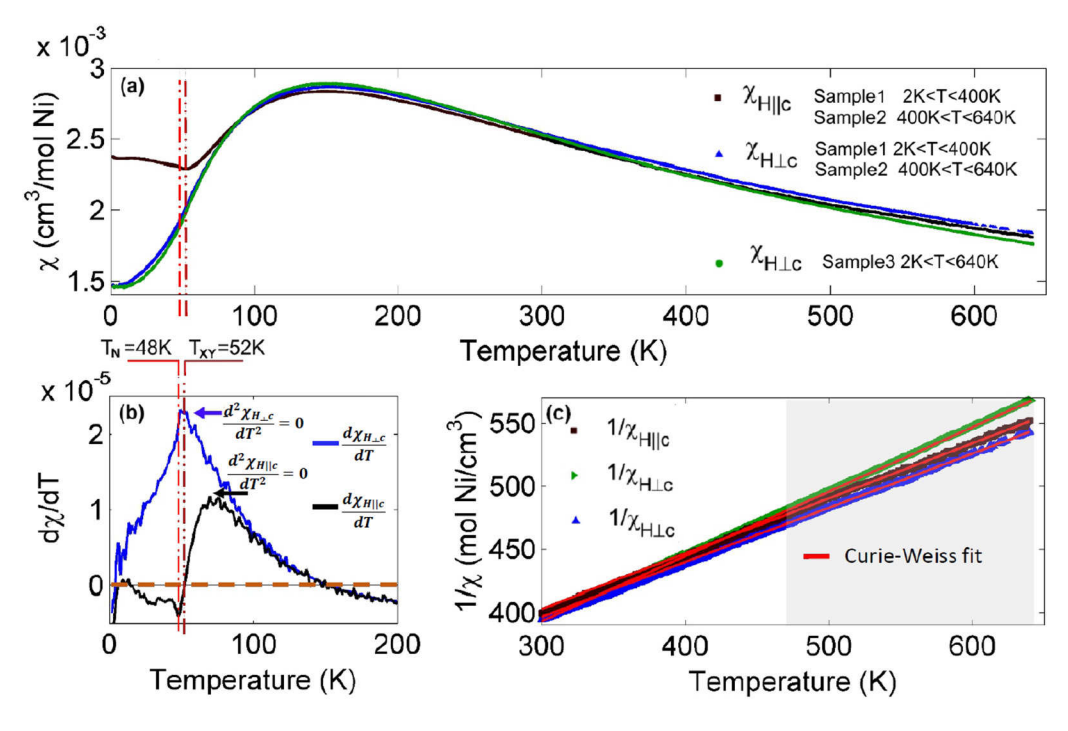


FIG. 2. (a) Single-crystal dc magnetic susceptibility data of $BaNi_2V_2O_8$ collected under a magnetic field of 1 T applied parallel and perpendicular with respect to the c axis. A Curie-impurity tail was subtracted from the data collected on sample 3. (b) The first derivative of $\chi_{H\parallel c}$ and $\chi_{H\perp c}$ with respect to temperature. (c) The inverse susceptibilities ($\chi_{H\parallel c}^{-1}$ and $\chi_{H\perp c}^{-1}$) plotted as a function of temperature and fitted using the Curie-Weiss law as described in the text. The fitted region lies within the shaded area.

an inflection point which is in agreement with the tiny feature observed at the same temperature in heat-capacity data [22] and suggests that the phase transition to the long-range magnetically ordered state occurs at $T_N = 48 \text{ K} \pm 0.5 \text{ K}$.

2. Curie-Weiss law

The magnetic susceptibility data were analyzed using the Curie-Weiss law $\chi(T) = \frac{C}{(T-\Theta_{\rm CW})}$ where C is the Curie constant and $\Theta_{\rm CW}$ is the Curie-Weiss temperature. Figure 2(c) shows the inverse magnetic susceptibilities plotted as a function of temperature over the range 300–640 K, the data are almost linear suggesting that BaNi₂V₂O₈ is in its paramagnetic regime. The Curie-Weiss law was fitted to each data set over the temperature range 470–640 K [solid red line in Fig. 2(c)] and the extracted values of the Curie-Weiss temperature and Curie constant were averaged over the different samples and directions of the applied magnetic field. The Curie-Weiss temperature and Curie constant of BaNi₂V₂O₈ were found to be $\Theta_{\rm CW} = -542 \pm 76$ K and $C = 1.06 \pm 0.12$ cm³ K/mol, respectively. The negative sign of the Curie-Weiss temperature confirms that the dominant magnetic exchange interaction in BaNi₂V₂O₈ is antiferromagnetic (AFM).

The Curie-Weiss temperature can be used to estimate the sum of the magnetic exchange interactions up to the third-neighbor interaction in $BaNi_2V_2O_8$ using the relation [31]

$$\Theta_{\text{CW}} = -\frac{S(S+1)(g-1)^2 \sum_{i=n,nn,nnn} z_i J_i}{3k_R}.$$
 (1)

Here, S=1 is the spin value, k_B is the Boltzmann constant, g is the Landé factor, and z_i is the number of neighbors coupled to each magnetic ion by the magnetic exchange interactions J_i . In the above relation, each interaction J_i is counted only once per bond. In BaNi₂V₂O₈, each Ni²⁺ magnetic ion has three first-nearest neighbors, six second-nearest neighbors, and three third-nearest neighbors [Fig. 1(a)], therefore, $\sum_{i=n,nn,nnn} z_i J_i = 3J_n + 6J_{nn} + 3J_{nnn} = 3J_{total}$ where J_{total} is defined as $J_{total} \equiv J_n + 2J_{nn} + J_{nnn}$. Substituting the extracted value of $\Theta_{\text{CW}} = -542 \pm 76$ K into Eq. (1) yields the value $J_{total} = 15 \pm 2$ meV.

3. Quenching of the orbital angular momentum

The Curie constant can be defined as $C = \frac{N_A \mu_B^2 \mu_{\rm eff}^2}{3k_B}$ where N_A is the Avogadro number, μ_B is the Bohr magneton, k_B is the Boltzmann constant, and $\mu_{\rm eff}$ is the effective moment of the magnetic ions. Using the value of the Curie constant $C = 1.06 \pm 0.12$ cm³ K/mol, extracted from the magnetic susceptibility data, the effective magnetic moment of the Ni²+ magnetic ions in BaNi₂V₂O₃ is found to be $\mu_{\rm eff} = 2.91 \pm 0.16$ $\mu_B/{\rm Ni²}^2$ +. This value is much lower than the theoretical value of $\mu_{\rm eff} = 5.59$ $\mu_B/{\rm Ni²}^2$ + calculated for the $3d^8$ electronic configuration of Ni²+ assuming unquenched orbital angular momentum, but is in good agreement with the value $\mu_{\rm eff} = 2.83$ $\mu_B/{\rm Ni²}^2$ + expected for the electronic configuration where the orbital angular momentum is quenched $(L=0, J=S=1, g_J=2)$. Such quenching is expected and commonly observed for the 3d ions in crystalline environments due to strong crystal-field effects [32].

B. Magnetic excitation spectrum of BaNi₂V₂O₈

1. Powder magnetic excitation spectrum

The magnetic excitations of $BaNi_2V_2O_8$ were explored using inelastic neutron scattering. First, to get an overview of the magnetic excitation spectrum and to estimate its energy range, INS data were collected on a powder sample at 5 K using the MERLIN time-of-flight spectrometer. The results are plotted on Fig. 3(a) as a function of energy and wave vector transfer, and reveal V-shaped spin-wave-type excitations which extend over the energy range 0–26 meV. The excitations have their first minimum at $|Q|=1.45 \text{ Å}^{-1}$ which corresponds to the proposed $(1,0,\frac{1}{2})$ magnetic Bragg peak position. A Van Hove singularity is observed at 26 meV, indicating the top of energy dispersion. The intensity of the excitations is strong at low wave vectors and decreases with increasing wave vector confirming their magnetic origins.

2. Single-crystal magnetic excitation spectrum within the honeycomb plane

Single-crystal INS measurements of BaNi₂V₂O₈ were performed using the PUMA thermal triple-axis spectrometer to explore the magnetic excitation spectrum within the honeycomb plane. The INS measurements were carried out at T = 3.5 K as a function of energy and wave vector along different high-symmetry directions within the (h,k,0)plane. Figure 4(a) shows the spectrum along the (0,k,0)direction which was constructed from a series of constant energy scans. The results reveal that the magnetic excitations of BaNi₂V₂O₈ consist of two spin-wave modes which both disperse from the magnetic Bragg peak positions and are consistent with the honeycomb lattice. The two modes are degenerate except at low energies. The dispersion along the (h, -2 - h, 0) direction [Fig. 4(b)] is similar to that along the (0,k,0) direction [Fig. 4(a)] as expected since these directions are equivalent due to the lattice symmetry. Figure 4(c) shows that the dispersion along the (h, -2h - 2, 0)direction has a modulation in the high-energy region which can be attributed to the presence of a weak second-neighbor

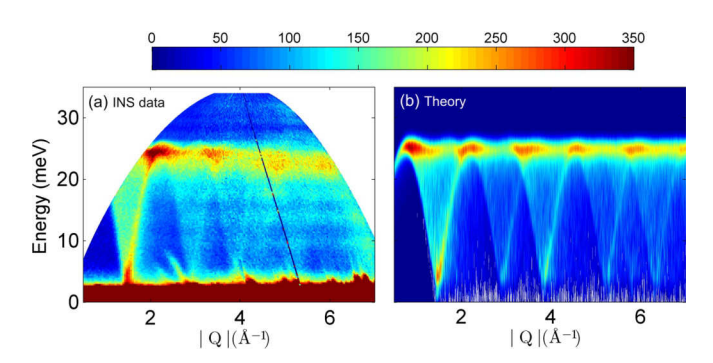


FIG. 3. (a) INS data measured on a powder sample at T=5 K using the Merlin spectrometer with an incident energy of 35 meV. (b) Spin-wave simulations of the powder excitation spectrum of $\mathrm{BaNi_2V_2O_8}$ performed for the Hamiltonian (3) with the parameters $J_n=12.3$ meV, $J_{nn}=1.25$ meV, $J_{nnn}=0.2$ meV, $J_{out}=-0.00045$ meV, $D_{EP}=0.0695$ meV, $D_{EA}=-0.0009$ meV.

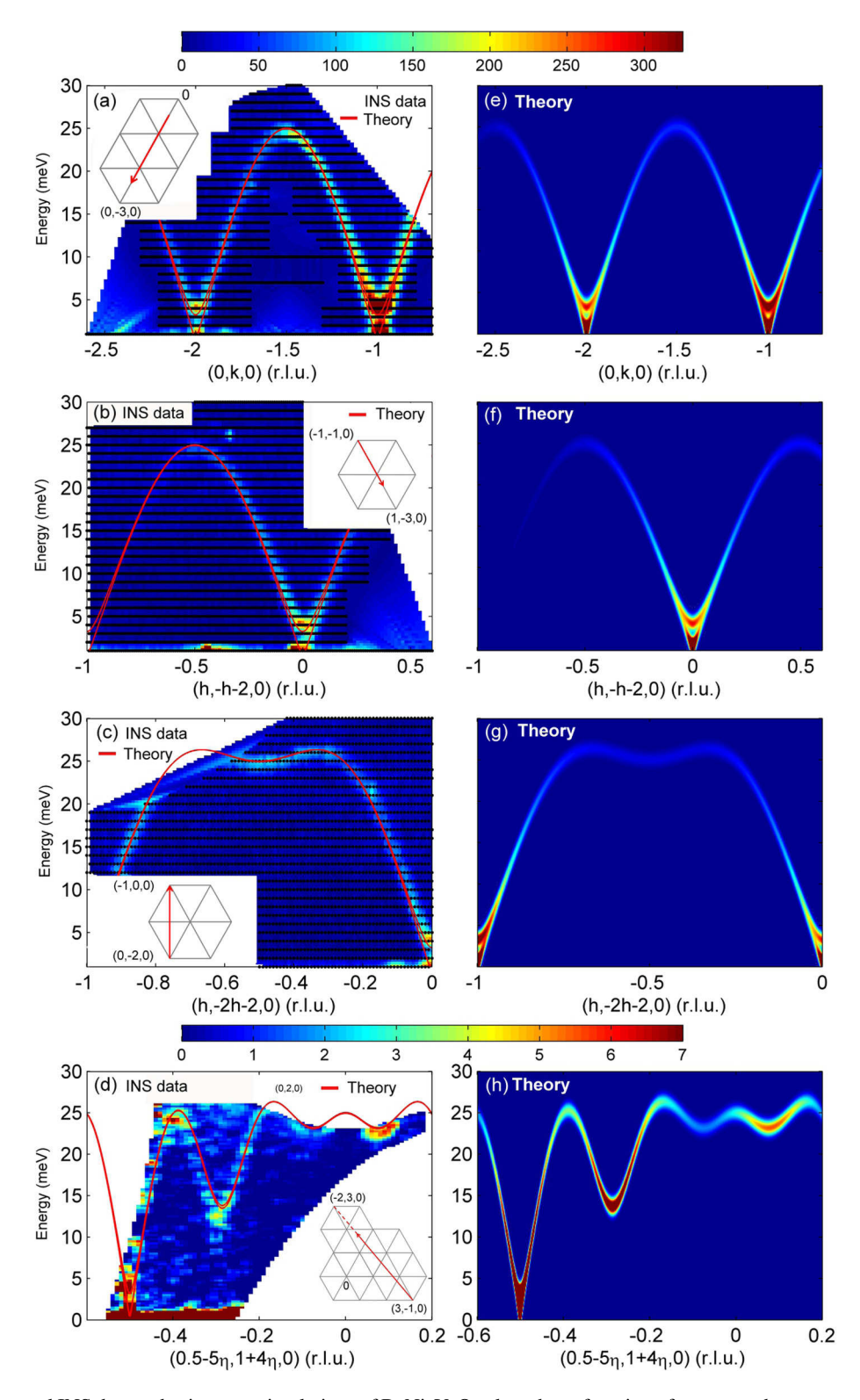


FIG. 4. Single-crystal INS data and spin-wave simulations of $BaNi_2V_2O_8$ plotted as a function of energy and wave vector transfer within the honeycomb plane. (a)–(c) INS data measured on the PUMA spectrometer at T=3.5 K along the directions (a) (0,k,0), (b) (h,-h-2,0), and (c) (h,-2h-2,0) as indicated by the red arrows in the insets. The black dotted lines indicate where the data were collected, features which appear outside these areas are artifacts and should be ignored. (d) Cut along the $(0.5-5\eta,1+4\eta,0)$ direction through the INS data collected at T=5 K on the cold-neutron multichopper LET spectrometer with incident energy of 30.2 meV. (e)–(h) Spin-wave simulations of the single-crystal magnetic cross section along the directions (e) (0,k,0), (f) (h,-h-2,0), (g) (h,-2h-2,0), and (h) $(0.5-5\eta,1+4\eta,0)$. The calculated spin-wave energies are represented by the solid red lines through the data on (a)–(d). All simulations were performed for the Hamiltonian (3) with the parameters $J_n=12.3$ meV, $J_{nn}=1.25$ meV, $J_{nnn}=0.2$ meV, $J_{out}=-0.00045$ meV, $D_{EP}=0.0695$ meV, $D_{EA}=-0.0009$ meV.

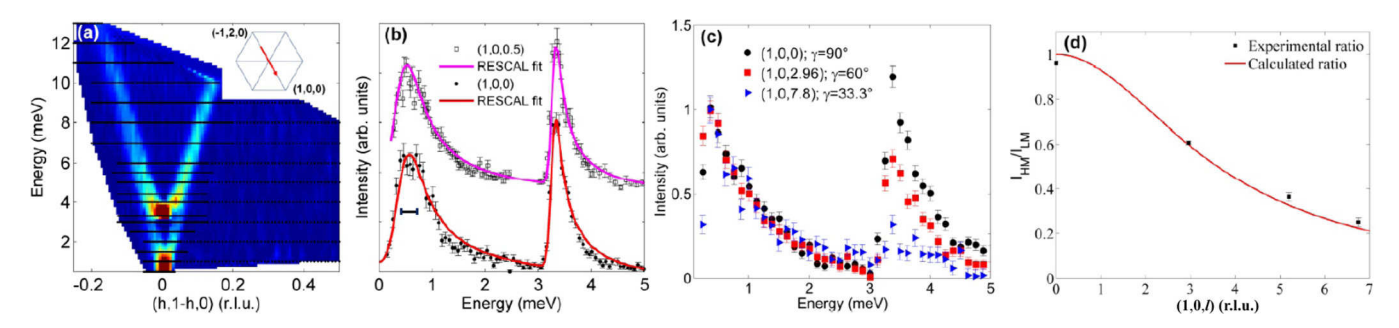


FIG. 5. Low-energy single-crystal INS data of $BaNi_2V_2O_8$. (a) INS measured on the PANDA spectrometer at T=4.3 K along the (h,1-h,0) direction, the black dotted lines indicate where the data were collected. (b) Energy scans at constant wave vectors of (1,0,0) (filled black circles) and (1,0,0.5) (open black squares) collected on the TASP spectrometer at T=1.47 K. The solid red and magenta lines represent the fit performed using the RESCAL software. The horizontal black lines represent the resolution broadening expected for a sharp mode. (c) Energy scans measured at T=4.3 K using the PANDA spectrometer at (1,0,l) where l is fixed to l=0 (filled black circles), l=2.96 (filled red squares), and l=7.8 (filled blue triangles). γ is the angle between the wave-vector transfer \vec{Q} and the c axis. The background has been substracted and the intensities have been scaled so that the amplitude of the lower-energy mode is fixed to 1. (d) The ratio of the intensity of the higher-energy mode to the lower-energy mode extracted experimentally from the PANDA data shown in (c) (filled black squares) and calculated using Eq. (2) (solid red line).

magnetic exchange interaction within the honeycomb plane as shown later.

To further explore the magnetic excitation spectra of $BaNi_2V_2O_8$ along all directions including off-symmetry directions, single-crystal INS measurements were also performed on the high-resolution cold-neutron multichopper LET spectrometer at the base temperature of T=5 K. These results confirm the data which were collected on the PUMA spectrometer along specific high-symmetry directions and, furthermore, provide additional data along low-symmetry directions such as that shown in Fig. 4(d).

To explore the low-energy magnetic excitation spectrum of $BaNi_2V_2O_8$ in detail, single-crystal INS measurements were carried out within the (h,k,0) scattering plane using the cold-neutron PANDA spectrometer. High-resolution constant energy scans were measured at T=4.3 K along the (h,1-h,0) direction over the energy range of 0–13 meV with energy steps of 0.5 meV. The results are plotted in Fig. 5(a) and confirm the presence of two spin-wave modes dispersing from (0,1,0). A high-resolution energy scan was performed at the dispersion minimum (1,0,0), at T=1.5 K using the cold-neutron TASP spectrometer. The result is plotted in Fig. 5(b) and shows two peaks corresponding to the two spin-wave modes. The data clearly reveal that both modes are gapped.

In order to obtain accurate values of these two energy gaps, the constant wave vector scan at the dispersion minimum (1,0,0) was fitted using the RESCAL software which convolves the instrumental resolution function calculated from the instrument settings with the dispersion relations. The dispersion relations [33] calculated for the Heisenberg honeycomb antiferromagnet within linear spin-wave theory were found to be appropriate to describe the magnetic excitations of $BaNi_2V_2O_8$. Energy gaps were introduced to the spin-wave dispersion relations [33] in order to reproduce the gaps observed experimentally. The fit to the energy scan at (1,0,0) is given by the solid red line in Fig. 5(b) and provides good agreement with the experimental INS data. The low-energy mode is found to be substantially broader than the

instrumental broadening (represented by the horizontal black line) due to the presence of the several split modes as will be shown later (see Sec. III C). The higher-energy mode is resolution limited. The fitted values of the energy gaps were found to be $E_1 = 0.41 \pm 0.03$ meV and $E_2 = 3.25 \pm 0.03$ meV for the lower- and higher-energy modes, respectively.

3. Anisotropy of the spin fluctuations

The presence of gapped magnetic excitations in the spin-wave spectra is often an indication of anisotropy because it suggests that there is a finite energy cost for the spins to fluctuate along specific crystallographic directions. The presence of two gapped modes at the in-plane antiferromagnetic-zone center suggests that $BaNi_2V_2O_8$ has both easy-plane and easy-axis anisotropies. One of the gapped spin-wave modes is probably due to spin fluctuations within the honeycomb plane perpendicular to the ordering direction which must overcome the easy-axis anisotropy, while the other is due to the fluctuations along the out-of-plane (c-axis) direction which must overcome the easy-plane anisotropy. Since the two modes have different gap sizes, the two anisotropies have different strengths.

The intensity variation of the modes at their gap energies as a function of wave-vector transfer can be used to verify the type of spin fluctuations to which they correspond. Indeed, the magnetic INS cross section depends on the direction of the wave-vector transfer $\vec{\mathbf{Q}}$ with respect to the direction of the spin fluctuations $\Delta \vec{\mathbf{S}}$ so that only the components of the spin fluctuations which are perpendicular to the wave vector transfer will contribute to the neutron scattering cross section.

To explore the origins of the observed energy gaps, constant wave-vector scans were measured at (1,0,l) over the energy range 0 to 7 meV at different fixed values l=0, 2.96, 5.2, 6.75, 7.8. The data were collected at 4.3 K using the PANDA spectrometer. Figure 5(c) shows the constant wavevector scans at (1,0,0), (1,0,2.96), and (1,0,7.8). To simplify the comparison, each energy scan has been rescaled so that the intensity of the lower-energy mode is 1. The results reveal that the amplitude of the high-energy mode decreases as the wave-

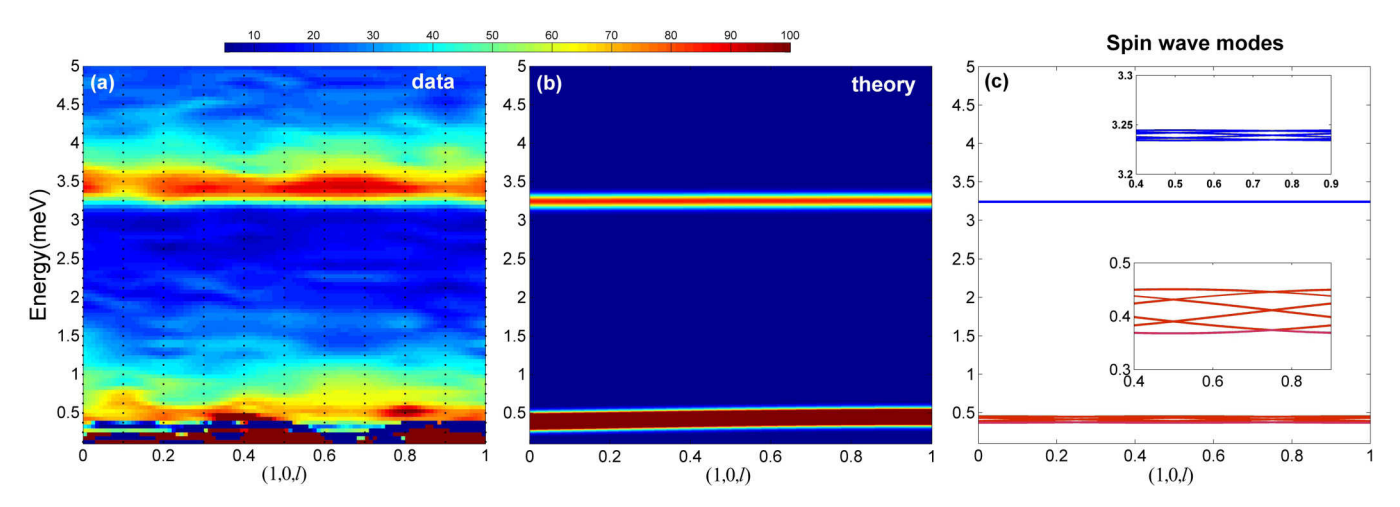


FIG. 6. (a) Single-crystal INS data of BaNi₂V₂O₈ measured on the PANDA spectrometer at T=4.3 K. The constant wave-vector scans were performed at (1,0,l) over the energy range of 0–5 meV with l fixed at values from 0 to 1 in steps of 0.1 to cover one Brillouin zone. (b) Spin-wave simulations of the single-crystal magnetic cross section along the (1,0,l) direction convolved with a Gaussian function. The simulations were performed for the Hamiltonian (3) with the parameters $J_n=12.3$ meV, $J_{nn}=1.25$ meV, $J_{nnn}=0.2$ meV, $J_{out}=-0.00045$ meV, $D_{EP}=0.0695$ meV, $D_{EA}=-0.0009$ meV. (c) The calculated dispersion relation of the 12 spin-wave modes along the (1,0,l) direction. The insets show the an enlarged representation of the dispersions of the six higher- and six lower-energy spin-wave modes, respectively.

vector transfer becomes increasingly parallel to the c axis. Indeed, both modes have approximately the same intensities at (1,0,0), where the wave-vector transfer lies entirely within the honeycomb plane. In contrast, for the energy scan at (1,0,7.8) where the wave vector transfer is mostly along the l direction, the high-energy mode almost disappears. These results suggest that the higher-energy mode is caused by out-of-plane spin fluctuations parallel to the c axis, while the lower-energy mode is due to in-plane spin fluctuations.

To quantitatively analyze this observed wavevector dependence, the ratio of the intensity of the higher-energy mode (I_{HM}) to the lower-energy mode (I_{LM}) for the constant wave vector scans at (1,0,0), (1,0,2.96), (1,0,5.2) and (1,0,6.75) was extracted and plotted as a function of l in Fig. 5(d). The constant wave vector scan at (1,0,7.8) was not analyzed because the higher-energy mode is extremely weak. The result reveals that this ratio continuously decreases as l increases from l=0 to 6.75.

The experimental wavevector dependence of the ratio $\frac{I_{HM}}{I_{LM}}$ was compared with the theoretical ratio $\frac{I_c}{I_{(a,b)}}$ of the intensities of the modes due out-of-plane (I_c) and in-plane $(I_{(a,b)})$ spin fluctuations for the magnetic structure of BaNi₂V₂O₈ taking account of the in-plane twinning (see Appendix):

$$\frac{I_c}{I_{(a,b)}} \propto \frac{[1 - \cos^2(\gamma)]}{\left\{1 - \left[\frac{1}{3}\sin^2(\gamma) + \frac{2}{3}\sin^2(\gamma)\cos^2(60)\right]\right\}},\tag{2}$$

where γ is the angle between the wave-vector transfer \mathbf{Q} and the c^* axis and is given by the relation $\tan(\gamma) = \frac{ch}{al\cos(30)}$ where a,c are the lattice constants. The solid red line in Fig. 5(d) shows the ratio of intensities calculated using the Eq. (2) with h fixed to h=1 and plotted as a function of l. The calculated l dependence of the ratio from l=0 to 7 is in good agreement with the l dependence of $\frac{l+M}{l}$ observed experimentally.

with the l dependence of $\frac{I_{HM}}{I_{LM}}$ observed experimentally. These results confirm that the higher-energy mode is caused by spin fluctuations along the c axis while the lower-energy mode is due to the fluctuations within the honeycomb plane.

The excitations which fluctuate along the c axis are gapped because the easy-plane anisotropy makes it energetically unfavorable for spins to have a component along the c direction. The presence of a gap for the in-plane excitations suggests the existence of an additional weak easy-axis anisotropy which establishes the spin-ordering direction within the ab plane. Because of the threefold crystal symmetry of $BaNi_2V_2O_8$ there should actually be three easy axes within the ab plane which give rise to three magnetic twin domains in the ordered phase.

4. Single-crystal magnetic excitation spectrum in the out-of-plane direction

To investigate the magnetic exchange interactions between the honeycomb layers, INS measurements were performed along the out-of-plane direction using the cold-neutron spectrometers PANDA and TASP. Figure 6(a) shows constant wave-vector scans at (1,0, l) over the energy range 0-5 meV where l was fixed at values from 0 to 1 in step of 0.1, thus, giving one Brillouin zone. The strong elastic signal at $(1,0,\frac{1}{2})$ corresponds to the magnetic Bragg peak while the elastic signal at (1,0,1) is due to a nuclear Bragg peak. The inelastic signals at \approx 0.5 meV and \approx 3.5 meV are the in-plane and out-of-plane spin-wave modes discussed in the previous section. The data clearly reveal that the upper energy mode is dispersionless within the experimental resolution. However, it is difficult to judge unambiguously whether or not the low-energy mode is dispersionless because of the strong contamination from the elastic scattering.

To investigate the dispersion of the low-energy mode in more detail, a constant wave-vector scan at $(1,0,\frac{1}{2})$ was measured and compared to the constant wave-vector scan at (1,0,0). Indeed, if the low-energy mode disperses along the c axis, the peak positions in the constant wave-vector scans at different wave-vector transfers would be shifted with respect to each other. Figure 5(b) shows the constant wave-vector scan at $(1,0,\frac{1}{2})$ (open black squares) where the elastic contribution

from the $(1,0,\frac{1}{2})$ magnetic Bragg peak and the flat background were subtracted. The magenta line in Fig. 5(b) presents the fit using the RESCAL software which takes into account the instrumental resolution. The fitted peak positions are $E_1 = 0.38 \pm 0.03$ meV and $E_2 = 3.25 \pm 0.03$ meV for the energy scan at $(1,0,\frac{1}{2})$ which are the same within the error as the peak positions of $E_1 = 0.41 \pm 0.03$ meV and $E_2 = 3.25 \pm 0.03$ meV observed in the energy scan at (1,0,0). The tiny energy shift of 0.03 meV in the position of the low-energy mode can be attributed either to resolution effects or to weak modulations due to the presence of an extremely small interplane coupling. These results reveal that both modes are dispersionless along the out-of-plane direction within the experimental resolution, implying that the magnetic exchange interactions between the honeycomb layers are extremely weak despite the presence of the long-range magnetic order.

C. Hamiltonian of BaNi₂V₂O₈

In order to extract the values of the magnetic exchange interactions and to determine the anisotropy of BaNi₂V₂O₈, the magnetic excitation spectrum of this compound was compared to the spectrum calculated using linear spin-wave theory. The general Hamiltonian given by Eq. (3) was assumed where J_n , J_{nn} , and J_{nnn} are the nearest-, second-nearest-, and third-nearest-neighbor isotropic Heisenberg magnetic exchange interactions, respectively, within the honeycomb plane, and J_{out} is an interplane exchange coupling (see Fig. 1). The interplane coupling was introduced because the magnetic structure of BaNi₂V₂O₈ develops long-range magnetic order below the transition temperature $T_N = 48$ K. The terms D_{EP} and D_{EA} describe the easy-plane and easy-axis single-ion anisotropies of the Ni²⁺ magnetic ions, respectively, where the easy-axis anisotropy lies within the ab plane. They are required to reproduce the energy gaps observed experimentally in the constant wave-vector scans at the dispersion minima (see

$$H = \sum_{i>j} J_n \cdot S_i \cdot S_j + \sum_{i>j} J_{nn} \cdot S_i \cdot S_j$$

$$+ \sum_{i>j} J_{nnn} \cdot S_i \cdot S_j + \sum_{i>j} J_{out} \cdot S_i \cdot S_j$$

$$+ \sum_{i>j} D_{EP} \cdot S_i^{c^2} + \sum_{i>j} D_{EA} \cdot S_i^{a^2}. \tag{3}$$

This Hamiltonian is similar to the Hamiltonians used to describe the related compounds $BaNi_2(PO_4)_2$ and $BaNi_2(AsO_4)_2$, where single-ion anisotropy rather than exchange anisotropy was assumed as is appropriate for the Ni^{2+} ion in an octahedral environment. The spin-wave simulations were performed for this proposed Hamiltonian using the SPINW MATLAB library [30]. The directions of the spins in their ground state were input into the SPINW calculation as fixed parameters based on the magnetic structure of $BaNi_2V_2O_8$ [Fig. 1(a)] proposed in the literature [21]. The initial signs of the exchange parameters J_n , J_n , J_{nnn} , J_{out} were chosen to be consistent with this magnetic structure and their initial values were chosen to be roughly compatible with the constraint $J_{total} = J_n + 2J_{nn} + J_{nnn} = 15 \pm 2$ meV extracted

from the dc susceptibility measurements [Eq. (1)]. The easy-plane anisotropy was given a positive sign $(D_{EP} > 0)$ to encourage the spins to lie within the honeycomb layers (ab) plane). The easy-axis anisotropy was given a negative sign $(D_{EA} < 0)$ and to encourage the spins to point along a particular direction within the honeycomb plane. Because of the threefold rotational symmetry of the lattice of $BaNi_2V_2O_8$ about the c axis, there are in fact three equivalent easy axes within the honeycomb plane rotated by 120° with respect to each other. Thus, below T_N we expect there to be three twins with spins lying along these three different easy axes. Each spin-wave simulation was performed for all three twins and the results were averaged assuming that the twins have equal weights.

The simulations were performed iteratively varying the values of J_n , J_{nnn} , J_{nnn} , J_{out} , D_{EP} , D_{EA} about various sets of initial parameters and comparing the results to the data. The parameters J_n , J_{nn} , J_{nnn} were found to be strongly coupled so that the range of the solutions for each of these parameters depends strongly on the values of the other parameters. To extract the whole range of possible solutions, the parameters were varied manually taking into account their strong coupling. The agreement of the extracted solutions with the experimental data was checked by comparing the excitations observed in BaNi₂V₂O₈ [Figs. 4(a)–4(d)] with the calculated spin-wave energies [solid red line over the data in Figs. 4(a)–4(d)] and calculated intensities [Figs. 4(e)–4(h)]. Finally, the range of the extracted solutions was restricted to be compatible with the constraint $J_{total} = 15 \pm 2$ meV.

The extracted solutions reveal that the first-nearest-neighbor magnetic exchange interaction J_n is the dominant interaction with values in the range of 11.3 meV $\leq J_n \leq$ 13.35 meV. The positive sign reveals that J_n is antiferromagnetic and is compatible with the proposed magnetic structure [Fig. 1(a)]. The second-nearest-neighbor interaction J_{nn} is sizable and lies in the range 0.85 meV $\leq J_{nn} \leq$ 1.5 meV. The presence of J_{nn} is necessary to reproduce the weak modulation observed experimentally at the top of the dispersion along the (h, -2h - 2, 0) direction [Fig. 4(c)]. J_{nn} is found to be antiferromagnetic implying that it competes with J_n and produces a weak frustration in the magnetic system.

The third-neighbor interaction $J_{\rm nnn}$ is small. It varies within the range $-0.1~{\rm meV} \leqslant J_{\rm nnn} \leqslant 0.4~{\rm meV}$ and can be either FM or AFM. The presence of $J_{\rm nnn}$ only provides a small improvement in the agreement with the experimental data and is not necessary to reproduce the observed spectrum. It was introduced to estimate the order of magnitude of other possible long-range interactions and their effect on the values of J_n and J_{nn} . Indeed, the presence of an AFM $J_{\rm nnn}$ increases the possible solutions of J_n and J_{nn} to the ranges $10.90~{\rm meV} \leqslant J_n \leqslant 13.35~{\rm meV}$ and $0.85~{\rm meV} \leqslant J_{nn} \leqslant 1.65~{\rm meV}$, respectively.

The anisotropy gives rise to the energy gaps of the two spin-wave modes at the antiferromagnetic zone center [e.g., at (1,0,0), Fig. 5(b)], and the values of the anisotropy parameters can be extracted from the sizes of these energy gaps. The easy-plane anisotropy D_{EP} must lie within the range 0.0635 meV $\leq D_{EP} \leq 0.0770$ meV to reproduce the gap of $E_2 = 3.25 \pm 0.03$ meV in the higher-energy mode

which corresponds to out-of-plane spin fluctuations, while the easy-axis anisotropy D_{EA} must be within the range $-0.0011~\text{meV} \leqslant D_{EA} \leqslant -0.0009~\text{meV}$ to reproduce the gap of $E_1 = 0.41 \pm 0.03~\text{meV}$ in the lower-energy mode.

The magnetic exchange coupling between the honeycomb layers was assumed to be realized via one of three possible magnetic exchange paths J_{out1} , J_{out2} , or J_{out3} which were discussed in the Introduction and represented in Fig. 1(b) by the dashed-dotted orange, dotted green, and solid cyan lines, respectively. The upper limit for each interplane coupling was extracted by simulating the magnetic excitation spectra of $\text{BaNi}_2\text{V}_2\text{O}_8$ taking into account the conditions that (i) the upper mode is dispersionless in the out-of-plane direction within the resolution error and (ii) the energy shift of the lower mode at (1,0,0) with respect to $(1,0,\frac{1}{2})$ does not exceed the experimentally observed value of 0.03 meV (see Sec. III B 2).

The results reveal that $J_{\rm out1}$ is ferromagnetic and must satisfy the condition $J_{\rm out1} \geqslant -0.00045$ meV, while $J_{\rm out2}$ and $J_{\rm out3}$ are antiferromagnetic and must satisfy $J_{\rm out2} \leqslant 0.00005$ meV and $J_{\rm out3} \leqslant 0.0012$ meV, respectively, in order to comply with the conditions (i) and (ii). Although $J_{\rm out1}$ and $J_{\rm out2}$ are characterized by the similar distances between Ni²⁺ ions, the upper limit of $J_{\rm out2}$ is nine times weaker than that of $J_{\rm out1}$. However, the effective contribution of $J_{\rm out2}$ to the interplane coupling is comparable to that of $J_{\rm out1}$ because there are six $J_{\rm out2}$ paths per Ni²⁺ magnetic ion in contrast to a single $J_{\rm out1}$. Although $J_{\rm out3}$ can have the largest value, it is unlikely to be responsible for the long-range magnetic order due to its large Ni²⁺-Ni²⁺ distance.

Figures 3(b) and 4(e)-4(h)show the powder single-crystal magnetic excitation and spectra of BaNi₂V₂O₈ simulated for the Hamiltonian $J_n = 12.3 \text{ meV},$ parameters with the $J_{nn} = 1.25 \text{ meV}, \quad J_{nnn} = 0.2 \text{ meV}, \quad J_{out1} = -0.00045 \text{ meV},$ $D_{EP} = 0.0695 \text{ meV}, \quad D_{EA} = -0.0009 \text{ meV}, \quad \text{respectively.}$ These values lie in the middle of the ranges of possible solutions. The simulations show good agreement with the experimental data. The simulated powder spectra [Fig. 3(b)] extends up to 26 meV and displays the V-shaped cones of the magnon dispersions with the first minimum at $|Q| = 1.45 \text{ Å}^{-1} \pm 0.05 \text{ Å}^{-1}$ matching the experimental data [Fig. 3(a)]. The simulated single-crystal dispersions within the (h,k,0) scattering plane [Figs. 4(e)-4(h)] are also consistent with the data [Figs. 4(a)-4(d)] and the intensity modulations of the simulated modes are in good agreement with the magnetic structure factor observed experimentally. Figure 6(b) shows the simulated single-crystal spectrum calculated along the out-of-plane (1,0,l) direction which again accurately matches the experimental data [Fig. 6(a)].

The spin-wave calculations reveal that the magnetic excitation spectrum of $BaNi_2V_2O_8$ consists of the 12 modes which are shared between the two excitation branches observed in the data [Fig. 6(c)]. Within each branch, the modes are almost degenerate and are not resolved experimentally due to the finite instrumental energy resolution. The lower-energy band consists of the six spin-wave modes which extend over the energy range 0.38–0.45 meV at (1,0,l) [Fig. 6(c.2)]. This leads to the finite FWHM of the lower-energy peak observed experimentally in the constant wave-vector scan at (1,0,0)

TABLE I. The effective in-plane magnetic exchange interaction $J_{\rm eff}$ calculated for BaNi₂M₂O₈ (M=V,P,As) assuming that each bond is counted only once. The values of the interplane coupling $J_{\rm out1}$, ordering temperature T_N , easy-plane single-ion anisotropy D_{EP} (averaged value), anisotropy temperature $T_{\rm ani}$, and planar regime temperature $T_{\rm XY}$ are also given after scaling by $J_{\rm eff}$.

Compound	$J_{ ext{eff}}, (rac{J_{ ext{eff}}}{k_B})$	$\frac{J_{ m out}}{J_{ m eff}}$	$\frac{T_N}{J_{\mathrm{eff}}}$	$\frac{D_{EP}}{J_{\mathrm{eff}}}$	$\frac{T_{\rm ani}}{J_{\rm eff}}$	$\frac{T_{\rm XY}}{J_{\rm eff}}$
BaNi ₂ V ₂ O ₈	10 meV (≈116 K)	0.000045	0.4	0.007	0.7	0.45
$BaNi_2P_2O_8$	1.792 meV (≈20.8 K)	0.00009	1.18	0.337	1.5	
BaNi ₂ As ₂ O ₈	1.896 meV (≈22 K)		0.89	0.318	1.45	

[Fig. 5(b)]. The higher-energy excitation branch also consists of the six modes but their bandwidth along (1,0,l) is only ≈ 0.01 meV. This explains why the higher-energy peak in the constant wave-vector scan at (1,0,0) appears resolution limited [Fig. 5(b)].

IV. DISCUSSION

The observed magnetic properties of $BaNi_2V_2O_8$ can be compared to the magnetic properties of the related nickel-based S=1 honeycomb antiferromagnets $BaNi_2(PO_4)_2$ and $BaNi_2(AsO_4)_2$, which also have easy-plane anisotropy. Of particular interest is the comparison of their anisotropies and interlayer couplings, and also their Néel and anisotropy temperatures in order to determine the existence and extent of their various magnetic regimes. Because these compounds have different magnetic structures and exchange interactions [e.g., in $BaNi_2(PO_4)_2$ the strongest interaction is between third-nearest neighbor [19]] it is necessary to find a way to compare them that takes these differences into account.

For each compound, an effective first-neighbor magnetic exchange interaction $J_{\rm eff}$ is defined, which represents the three nearest-neighbor exchange interactions and is compatible with the magnetic structure. It is given by

$$J_{\text{eff}} = \frac{\sum_{i}^{3} (z_{i}^{+} |J_{i}| - z_{i}^{-} |J_{i}|)}{N_{\text{nearest}}},$$
 (4)

where $|J_i|$ is the absolute value of the exchange interaction between a magnetic ion and its ith-nearest neighbor, $N_{\rm nearest}$ is the number of first-neighbor magnetic ions which is $N_{\rm nearest}=3$ for a honeycomb lattice. z_i^+ and z_i^- are the numbers of bonds between a magnetic ion and its ith-nearest neighbors which reinforce and oppose the magnetic structure, respectively. In the case of BaNi₂V₂O₈, the first-and third-neighbor interactions J_n and $J_{\rm nnn}$ which are both AFM, reinforce the magnetic structure, because as shown in Fig. 1(a), first- and third-neighbor spins are aligned antiparallel at low temperatures ($z_n^+ = z_{\rm nnn}^+ = 3$ and $z_n^- = z_{\rm nnn}^- = 0$). On the other hand, the second-neighbor interaction J_{nn} , which is also AFM, opposes the structure because second-neighbor spins are parallel ($z_{nn}^+ = 0$ and $z_{nn}^- = 6$).

Table I summarizes the values of $J_{\rm eff}$ for BaNi₂M₂O₈ (M=V,P,As). The value for BaNi₂V₂O₈ is found to be $J_{\rm eff}\approx 10~{\rm meV}$ and was calculated using the

values of $J_n = 12.3 \text{ meV}$, $J_{nn} = 1.25 \text{ meV}$, and $J_{\text{nnn}} = 0.2 \text{ meV}$ extracted from fitting the magnetic excitation spectrum. The values of $J_{\text{eff}} = 1.792 \text{ meV}$ and $J_{\text{eff}} = 1.896 \text{ meV}$ for BaNi₂P₂O₈ and BaNi₂As₂O₈, respectively, were estimated using the corresponding magnetic structures and Hamiltonians reported in the literature [18,19].

The value of $J_{\rm eff}$ for BaNi₂V₂O₈ is much greater than the values for BaNi₂P₂O₈ and BaNi₂As₂O₈, therefore, to compare the important temperatures and interaction energies of BaNi₂V₂O₈ to those of the other compounds, these quantities are first scaled by J_{eff} as listed in Table I. The scaled interplane coupling in $BaNi_2V_2O_8$ ($J_{out} = 0.000045J_{eff}$) is weaker than in $BaNi_2P_2O_8$ ($J_{out} = 0.00009J_{eff}$). As a consequence, the ordering temperature $T_N = 0.4 J_{\text{eff}}/k_B$ in BaNi₂V₂O₈, is also suppressed in the relative scale with respect to $T_N = 1.18 J_{\text{eff}}/k_B$ and $T_N = 0.89 J_{\text{eff}}/k_B$ observed in BaNi₂P₂O₈ and BaNi₂As₂O₈, respectively. The scaled easyplane anisotropy in BaNi₂V₂O₈ $D_{EP} \approx 0.007 J_{\text{eff}}$ is much weaker than the values $D_{EP} \approx 0.337 J_{\mathrm{eff}}$ and $D_{EP} \approx 0.318 J_{\mathrm{eff}}$ estimated for BaNi₂P₂O₈ and BaNi₂As₂O₈, respectively. This leads to the appearance of anisotropic magnetic behavior in BaNi₂V₂O₈ at lower relative temperature than in the other two compounds. Indeed, anisotropic magnetism in BaNi₂V₂O₈ appears in the susceptibility at $T_{\rm ani} = 80$ K below which $\chi_{H\perp c}$ and $\chi_{H\parallel c}$ split, this corresponds to $T_{\rm ani}\approx 0.7J_{\rm eff}/k_B$ in the relative temperature scale. For comparison, in both BaNi₂P₂O₈ and BaNi₂As₂O₈, the $\chi_{H\perp c}$ and $\chi_{H\parallel c}$ start to split at $T_{\rm ani} = 32 \text{ K}$ [19] which in the relative temperature scale correspond to $T_{\rm ani} \approx 3J_{\rm eff}/k_B$ and $T_{\rm ani} \approx 2.9J_{\rm eff}/k_B$, respectively.

The experimental susceptibility of BaNi₂V₂O₈ can be compared with the results of quantum Monte Carlo (QMC) simulations performed by Cuccoli et al. [13,14] for the antiferromagnetic spin- $\frac{1}{2}$ 2D square lattice with weakly Ising (XXZ-type) interactions. Although the simulations do not include the interplane coupling or the easy-axis anisotropy, the qualitative agreement with $\chi_{H\perp c}$ and $\chi_{H\parallel c}$ of BaNi₂V₂O₈ is remarkable (see Fig. 1 of Ref. [14]). In particular, the QMC simulations predict that the in-plane and out-of-plane susceptibilities are isotropic at high temperatures but split from each other as temperature decreases, revealing anisotropic behavior. This is, indeed, what was observed in the experimental susceptibility of $BaNi_2V_2O_8$ below $T_{ani} = 80 \text{ K}$ $(T_{\rm ani} \approx 0.7 J_{\rm eff}/k_B)$. Moreover, according to QMC simulations, the system displays a crossover to a regime where the easy-plane anisotropy dominates. This crossover manifests itself as a minimum at a finite temperature $T_{co} = 0.3 J_n/k_B$ below which the out-of-plane susceptibility reduces only a little and then becomes approximately constant while the in-plane susceptibility drops steadily [13,14]. This is in a good agreement with $\chi_{H\parallel c}$ in BaNi₂V₂O₈ which reveals a minimum at $T_{XY} = 0.45 J_{\text{eff}}/k_B$ in the relative scale ($T_{XY} =$ 52 K in absolute scale) and then increases slightly and becomes constant with further temperature decrease, in contrast to $\chi_{H\perp c}$, which decreases continuously. The minimum observed in the $\chi_{H\parallel c}$ of BaNi₂V₂O₈ at $T_{XY}=0.45J_{\text{eff}}/k_B$ (Fig. 2) can be assigned to the minimum at T_{co} predicted by QMC [13,14], implying a crossover to a regime where BaNi₂V₂O₈ displays strong 2D easy-plane anisotropy.

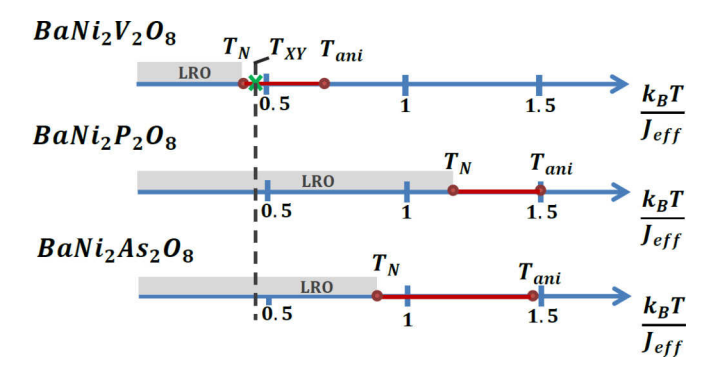


FIG. 7. The magnetic regimes of $BaNi_2V_2O_8$, $BaNi_2P_2O_8$, and $BaNi_2As_2O_8$ as a function of the relative temperature scale (k_BT/J_{eff}) . The Néel temperature T_N and the temperature T_{ani} where the magnetic anisotropy first appears are indicated by the red filled circles. The gray area below T_N indicates the long-range magnetically ordered phase. The temperature T_{XY} , at which $\chi_{H\parallel c}$ in $BaNi_2V_2O_8$ has a minimum associated with EP anisotropy regime, is marked by the green cross. The black dashed line indicates the position of T_{XY} with respect to $BaNi_2P_2O_8$ and $BaNi_2As_2O_8$.

It is remarkable that this characteristic minimum associated with a crossover to an easy-plane dominated regime is experimentally observed only in the $\chi_{H\parallel c}$ of BaNi₂V₂O₈ while susceptibilities of BaNi₂P₂O₈ and BaNi₂As₂O₈ reveal only the splitting of $\chi_{H\perp c}$ and $\chi_{H\parallel c}$ below $T_{\rm ani}$. It can be understood by comparing the value of T_N in BaNi₂V₂O₈, BaNi₂P₂O₈, and BaNi₂As₂O₈ in a relative temperature scale. Indeed, for all compounds, quasi-2D easy-plane anisotropy should be observable over the temperature range T_N - T_{ani} , while below T_N 3D magnetic behavior dominates and above $T_{\rm ani}$ the effect of the easy-plane anisotropy is overcome by the thermal energy. The value of T_{XY} for BaNi₂P₂O₈ and BaNi₂As₂O₈ can be expected to be similar to the value $T_{\rm XY} = 0.45 J_{\rm eff}/k_B$ extracted for BaNi₂V₂O₈. Because in both BaNi₂P₂O₈ and BaNi₂As₂O₈, $T_N \approx 1 J_{\text{eff}}/k_B$ lies at higher relative temperatures than $T_{XY} = 0.45 J_{\text{eff}}/k_B$, the easy-plane regime in these compounds is overcome by the long-range ordered phase as illustrated in Fig. 7 and the predicted minimum in $\chi_{H\parallel c}$ is not present in their susceptibility data

V. CONCLUSIONS

We have performed a comprehensive investigation of the novel spin-1, honeycomb, antiferromagnet $BaNi_2V_2O_8$ employing inelastic neutron scattering and dc susceptibility measurements. The observed low-temperature susceptibility data $\chi_{H\perp c}$ and $\chi_{H\parallel c}$ are in good agreement with the experimental results published previously [21] and reveal that $BaNi_2V_2O_8$ behaves as a quasi-2D Heisenberg antiferromagnet with easy-plane anisotropy.

The transition to long-range antiferromagnetic order is evident only as a subtle inflection point detected in $\chi_{H\parallel c}$ at $T_N=48~{\rm K}\pm0.5~{\rm K}$ in agreement with the weak features reported previously at the same temperature in both $\chi_{H\parallel c}$ [21] and heat-capacity data [22]. It is also consistent with the phase transition to the antiferromagnetic ordered state observed at

 $T_N = 47.5-47.75$ K by neutron diffraction measurements on the same crystals [34].

The crossover to the regime dominated by easy-plane anisotropy is observed in BaNi₂V₂O₈ at $T_{\rm XY}=52$ K and is characterized by a minimum in $\chi_{H\parallel c}$ (see Fig. 2) which is in agreement with the predictions of quantum Monte Carlo simulations performed for the $S=\frac{1}{2}$ 2D XXZ square lattice [13]. The corresponding relative temperature $T_{\rm XY}=0.45J_{\rm eff}/k_B$ is also found to be in general agreement with $T_{\rm XY}^{\rm QMC}\approx0.3J_n/k_B$ predicted by QMC.

analysis The of the high-temperature susceptibility data allows the Curie-Weiss temperature $\Theta_{\rm CW} = -542 \pm 76$ K and Curie constant to be extracted for the first time. The effective magnetic moment of the Ni²⁺ ion was estimated from the Curie constant and reveals that the orbital angular momentum of the magnetic Ni²⁺ ion is almost but not completely quenched. The fact that the orbital angular momentum is partially recovered indicates the presence of a weak spin-orbit coupling and is consistent with the single-ion anisotropy observed in this magnetic system [35].

The INS measurements reveal that BaNi₂V₂O₈ has magnetic spin-wave excitations which disperse within the honeycomb plane and are dispersionless (within resolution error) in the out-of-plane direction confirming that BaNi₂V₂O₈ is an almost ideal 2D magnetic system. The observed magnetic excitation spectrum of BaNi₂V₂O₈ consists of two gapped spin-wave branches due to in-plane and out-of-plane spin-wave fluctuations. The analysis of the relative intensities of these branches as a function of wave-vector transfer reveals that the lowerenergy branch is due to fluctuations within the honeycomb plane while the higher-energy branch is due to fluctuations along the c axis. The fact that the out-of-plane fluctuations have a significant energy gap confirms the presence of a dominant easy-plane anisotropy which makes these fluctuations energetically more costly to excite. The smaller energy gap of the in-plane spin fluctuations implies the presence of a weak easy-axis anisotropy within the honeycomb plane. The extracted values of the energy gaps $E_1 = 0.41 \pm 0.03$ meV and $E_2 = 3.25 \pm 0.03$ meV are in qualitative agreement with the values of $E_1 = 0.2 \text{ meV}$ and $E_2 = 3 \text{ meV}$ briefly mentioned in the paper by Knafo et al. [22]. However, since no data are shown, it is difficult to make a quantitative comparison with our results. Both the powder and single-crystal magnetic excitation spectra of BaNi₂V₂O₈ were reproduced well by linear spinwave theory allowing the Hamiltonian of BaNi₂V₂O₈ to be determined.

Both the powder and single crystal magnetic excitation spectra of $BaNi_2V_2O_8$ were reproduced well by linear spin-well theory allowing the Hamiltonian of $BaNi_2V_2O_8$ to be precisely determined. The solution reveals that the dominant term is the nearest-neighbor in-plane exchange interaction J_n , which is AFM and lies within the range of $10.9 \text{ meV} \leqslant J_n \leqslant 13.35 \text{ meV}$. This value of J_n is considerably larger than the value $J_1 \approx 8.3 \text{ meV}$ published by Rogado et al. [21] which was extracted from dc susceptibility using the high-temperature series expansion approach. The discrepancy can be attributed to the fact that the second-neighbor interaction was not considered and the data used for the comparison were collected at relatively low temperatures ($T \leqslant 300 \text{ K}$).

The second J_{nn} and third J_{nnn} neighbor in-plane interactions were found to be much smaller and to vary within the ranges of 0.85 meV $\leq J_{nn} \leq 1.65$ meV and -0.1 meV $\leq J_{nnn} \leq 0.4$ meV, respectively. J_{nn} is antiferromagnetic and opposes the magnetic structure of BaNi₂V₂O₈ introducing a weak frustration to the system. The third-neighbor interaction J_{nnn} is not necessary to reproduce the experimental data and represents the size of the contributions from distant neighbors.

The values the easy-plane and easyanisotropies extracted be within axis are $0.0635 \leqslant D_{EP} \leqslant 0.0770$ the ranges meV and $-0.0011 \leqslant D_{EA} \leqslant -0.0009 \text{ meV},$ respectively. The dominance of the easy-plane anisotropy over the easy-axis anisotropy confirms the planar character of the magnetism in this compound. Although BaNi₂V₂O₈ displays long-range magnetic order, the interplane coupling J_{out} was found to be surprisingly small and to vary within the energy range $-0.00045 \text{ meV} \leqslant J_{\text{out}} \leqslant 0.0012 \text{ meV}$ where the sign of the J_{out} depends on the exchange path responsible for this coupling. The very weak J_{out} explains the absence of clear signatures of the transition to long-range magnetic order in the dc susceptibility and heat-capacity [22] data. The presence of the long-range magnetic order despite such a weak interplane coupling can be attributed to the presence of weak easy-axis anisotropy. Indeed, Knafo et al. [22] demonstrate the importance of the easy-axis anisotropy for inducing the long-range magnetically ordered state in BaNi₂V₂O₈ by exploring the effects of the field- and pressure-induced anisotropies on the ordering temperature T_N . Thus, a combination of a very weak interplane coupling and a very weak easy-axis anisotropy may together be sufficient to induce long-range magnetic order at the finite temperature of $T_N = 48 \pm 0.5$ K in this planar antiferromagnet.

To summarize, $BaNi_2V_2O_8$ is a highly 2D antiferromagnet with dominant easy-plane anisotropy and is, thus, a promising candidate for the further investigation of BKT behavior [23,24]. The temperature region T_N - T_{XY} , where the easy-plane anisotropy dominates but which is above the transition to 3D order, is especially interesting for the observation of vortex excitations and BKT phenomena.

ACKNOWLEDGMENTS

The susceptibility measurements were performed at the Core Lab for Quantum Materials, HZB; we thank K. Siemensmeyer for helping with these measurements. We also thank S. Toth for his help with the SPINW simulations. M.M. was partly supported by Marie Sklodowska Curie Action, International Career Grant through the European Commission and Swedish Research Council (VR), Grant No. INCA-2014-6426 as well as a VR neutron project grant (BIFROST, Grant No. Dnr. 2016-06955).

APPENDIX

In this appendix, the ratio of the neutron scattering intensities of the two spin-wave modes at (1,0,l) in $BaNi_2V_2O_8$ is calculated as a function of wave vector l. This calculation takes into account the known magnetic structure of this compound

and is averaged of the three magnetic twin domains. The results are used in Sec. III B 2 to verify the fluctuation directions of the two spin-wave modes and provide quantitative agreement with the data.

Figure 8(a) shows the direction of the spins in BaNi₂V₂O₈ within the honeycomb (*ab*) plane below T_N . The thick magenta, red, and green arrows labeled $\vec{s_1}$, $\vec{s_2}$, and $\vec{s_3}$, respectively, indicate the spin directions of the three twins. The local coordinate systems $\tilde{x}_n, \tilde{y}_n, \tilde{z}_n$ (n=1,2,3) for all three twins are also plotted using the same color coding. Each coordinate system is constructed so that $\tilde{x}_n \parallel \vec{s_n}, \tilde{y}_n \perp \vec{s_n}, \tilde{z} = \tilde{x} \times \tilde{y}$, and $\tilde{z}_n \parallel c$ axis. For each twin, the neutron scattering cross section is proportional to the relation [36]

$$\begin{split} I &\propto \left(1 - \hat{q}_{\tilde{x}}^2\right) \cdot S^{\tilde{x}\tilde{x}}(Q, w) + \left(1 - \hat{q}_{\tilde{y}\tilde{y}}^2\right) \cdot S^{\tilde{y}\tilde{y}}(Q, w) \\ &+ \left(1 - \hat{q}_{\tilde{z}}^2\right) \cdot S^{\tilde{z}\tilde{z}}(Q, w). \end{split} \tag{A1}$$

Here, \hat{q} is a unit vector in the direction of \vec{Q} and $\hat{q}_{\bar{x}}$, $\hat{q}_{\bar{y}}$, $\hat{q}_{\bar{z}}$ are its components within the local coordinate system $\tilde{x}, \tilde{y}, \tilde{z}$ of that twin. In the ordered phase the first term in Eq. (A1) is responsible for the elastic magnetic signal, while the second and third terms give the intensity of the inelastic neutron scattering due to spin fluctuations perpendicular to the

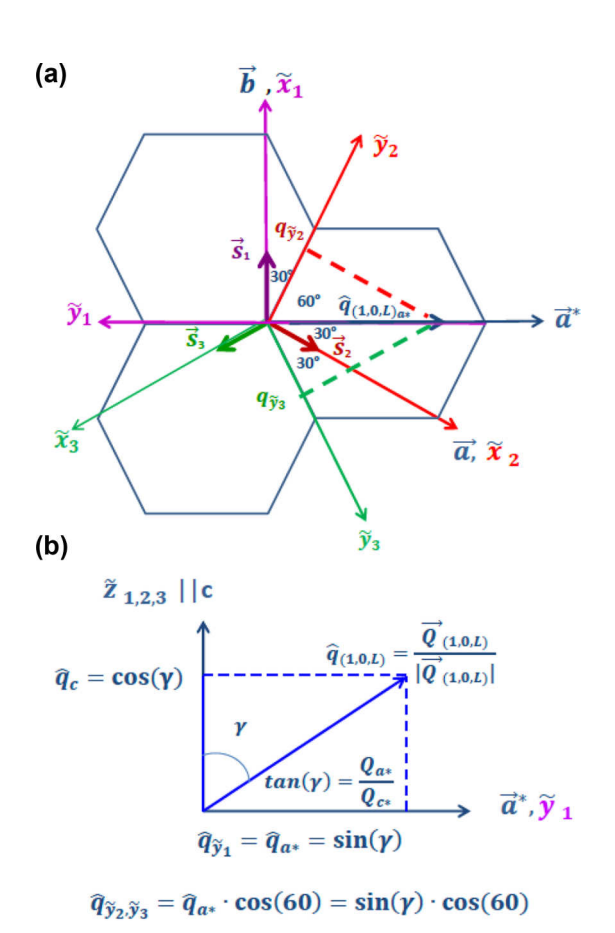


FIG. 8. (a) Magnetic structure of $BaNi_2V_2O_8$ in the honeycomb plane. The spin (thick arrows) and coordinate systems (thin arrows) for the three twinned domains are indicated by the magenta, red, and green colors, respectively. The projection of the (1,0,l) wave-vector transfer onto the spin direction of each twin is also shown. (b) A sketch of the $a^\star c^\star$ plane and wave-vector transfer \vec{Q} .

order along the \tilde{y} and \tilde{z} directions. Therefore, the ratio of the intensities $I_{\tilde{z}}$ and $I_{\tilde{y}}$ of the modes due to the spin fluctuations along the \tilde{y} and \tilde{z} directions, respectively, is proportional to

$$\frac{I_{\tilde{z}}}{I_{\tilde{y}}} \propto \frac{\left(1 - \hat{q}_{\tilde{z}}^2\right)}{\left(1 - \hat{q}_{\tilde{y}}^2\right)}.\tag{A2}$$

If there are domains, the terms $\hat{q}_{\tilde{z}}^2$ and $\hat{q}_{\tilde{y}}^2$ in Eq. (A1) should be replaced by their averaged values over the domains $\langle \hat{q}_{\tilde{z}}^2 \rangle$ and $\langle \hat{q}_{\tilde{z}}^2 \rangle$.

In BaNi₂V₂O₈, \tilde{z}_n is parallel to the c axis for all twins so that $\hat{q}_{\tilde{z}_1} = \hat{q}_{\tilde{z}_2} = \hat{q}_{\tilde{z}_3} = \hat{q}_c$ where \hat{q}_c is the projection of the unit wave vector \hat{q} on the c axis. Thus, the ratio of the scattering intensities I_c and $I_{(a,b)}$, due to spin-fluctuations along the c-axis and within the honeycomb plane, respectively, is proportional to

$$\frac{I_c}{I_{(a,b)}} \propto = \frac{\left(1 - \hat{q}_c^2\right)}{\left(1 - \langle \hat{q}_{\bar{v}}^2 \rangle\right)}.$$
 (A3)

The projection \hat{q}_c of the unit wave vector \hat{q} on the c axis and its averaged value over the twins are given by

$$\hat{q}_c = \cos(\gamma),$$

 $\langle \hat{q}_c^2 \rangle = \cos^2(\gamma),$ (A4)

where γ is the angle between the wave-vector transfer \vec{Q} and the c axis which is $\gamma = a \tan(\frac{Q_{a^*}}{Q_{c^*}})$ where $Q_{a^*} = \frac{2\pi h}{a \cos(30)}$ and $Q_{c^*} = \frac{2\pi l}{a \cos(30)}$ [see Fig. 8(b)].

 $Q_{c^*} = \frac{2\pi l}{c}$ [see Fig. 8(b)]. The projection of \hat{q} on the \tilde{y}_n axis can be found for each twin using the relation

$$\hat{q}_{\tilde{y}_n} = \hat{q}_{a^*} \cdot \cos(\beta_n) = \sin(\gamma)\cos(\beta_n), \tag{A5}$$

where β_n is the angle between the a^* axis and the \tilde{y}_n axis for the the *n*th twin. As shown in Fig. 8(a), $\beta_1 = 180^\circ$, $\beta_2 = 60^\circ$, and $\beta_3 = -60^\circ$ for the first, second, and third twins, respectively. Therefore, assuming that the three twins are equally populated,

$$\hat{q}_{\tilde{y}_{1}} = -\sin(\gamma),$$

$$\hat{q}_{\tilde{y}_{2}} = \hat{q}_{\tilde{y}_{3}} = \sin(\gamma)\cos(60),$$

$$\langle \hat{q}_{\tilde{y}}^{2} \rangle = \frac{1}{3}\sin^{2}(\gamma) + \frac{2}{3}\sin^{2}(\gamma)\cos^{2}(60).$$
(A6)

The ratio of the intensity of the mode due to the out-ofplane spin fluctuations (I_c) to the intensity of the mode due to in-plane spin fluctuations ($I_{(a,b)}$) averaged over all twins can be obtained by the substitution of Eqs. (A6) and (A4) into (A3) giving

$$\frac{I_c}{I_{(a,b)}} \propto \frac{[1 - \cos^2(\gamma)]}{\left\{1 - \left[\frac{1}{3}\sin^2(\gamma) + \frac{2}{3}\sin^2(\gamma)\cos^2(60)\right]\right\}}.$$
 (A7)

- [1] B. Lake, D. A. Tennant, C. D. Frost, and S. E. Nagler, Nat. Mater. 4, 329 (2005).
- [2] A. K. Bera, B. Lake, A. T. M. N. Islam, B. Klemke, E. Faulhaber, and J. M. Law, Phys. Rev. B 87, 224423 (2013).
- [3] S. Notbohm, P. Ribeiro, B. Lake, D. A. Tennant, K. P. Schmidt, G. S. Uhrig, C. Hess, R. Klingeler, G. Behr, B. Büchner *et al.*, Phys. Rev. Lett. 98, 027403 (2007).
- [4] V. L. Berezinskii, ZhETF 59, 907 (1971) [Sov. Phys.–JETP 32, 493 (1971)].
- [5] V. L. Berezinskii, ZhETF 61, 1144 (1972) [Sov. Phys.–JETP 34, 610 (1972)].
- [6] J. M. Kosterlitz and D. J. Thouless, J. Phys. C: Solid State Phys. 6, 1181 (1973).
- [7] J. M. Kosterlitz, J. Phys. C: Solid State Phys. 7, 1046 (1974).
- [8] N. D. Mermin and H. Wagner, Phys. Rev. Lett. 17, 1133 (1966).
- [9] Y. Xu and C. Zhang, Phys. Rev. Lett 114, 110401 (2015).
- [10] W. Zhao, Q. Wang, M. Liu, W. Zhang, Y. Wang, M. Chen, Y. Guo, K. He, X. Chen, Y. Wang *et al.*, Solid State Commun. **165**, 59 (2013).
- [11] D. J. Resnick, J. C. Garland, J. T. Boyd, S. Shoemaker, and R. S. Newrock, Phys. Rev. Lett. 47, 1542 (1981).
- [12] U. Tutsch, B. Wolf, S. Wessel, L. Postulka, Y. Tsui, H. Jeschke, I. Opahle, T. Saha-Dasgupta, R. Valenti, A. Brühl *et al.*, Nat. Commun. 5, 5169 (2014).
- [13] A. Cuccoli, T. Roscilde, V. Tognetti, R. Vaia, and P. Verrucchi, Phys. Rev. B 67, 104414 (2003).
- [14] A. Cuccoli, T. Roscilde, R. Vaia, and P. Verrucchi, Phys. Rev. Lett. 90, 167205 (2003).
- [15] A. R. Wildes, H. M. Rønnow, B. Roessli, M. J. Harris, and K. W. Godfrey, Phys. Rev. B 74, 094422 (2006).
- [16] H. M. Rønnow, A. R. Wildes, and S. T. Bramwell, Physica B: Condensed Matter **276**, 676 (2000).
- [17] L. P. Regnault, J. Y. Henry, J. Rossat-Mignod, and A. De Combarieu, J. Magn. Magn. Mater. 15–18, 1021 (1980).
- [18] L. P. Regnault, J. P. Boucher, J. Rossat-Mignod, J. Bouillot, R. Pynn, J. Y. Henry, and J. P. Renard, Phys. B+C (Amsterdam) 136, 329 (1986).

- [19] L. P. Regnault and J. Rossat-Mignod, in *Magnetic Properties of Layered Transition Metal Compounds*, edited by L. J. d. Jongh (Kluwer Academic, Netherlands, 1990).
- [20] P. Sengupta, A. W. Sandvik, and R. R. P. Singh, Phys. Rev. B 68, 094423 (2003).
- [21] N. Rogado, Q. Huang, J. W. Lynn, A. P. Ramirez, D. Huse, and R. J. Cava, Phys. Rev. B 65, 144443 (2002).
- [22] W. Knafo, C. Meingast, K. Grube, S. Drobnik, P. Popovich, P. Schweiss, P. Adelmann, T. Wolf, and H. v. Lohneysen, Phys. Rev. Lett. 99, 137206 (2007).
- [23] M. Heinrich, H.-A. Krug von Nidda, A. Loidl, N. Rogado, and R. J. Cava, Phys. Rev. Lett. 91, 137601 (2003).
- [24] D. Waibel, G. Fisher, T. Wolf, H. Löhneysen, and B. Pilawa, Phys. Rev. B 91, 214412 (2015).
- [25] R. I. Bewley, R. S. Eccleston, K. A. McEwen, S. Hayden, M. Dove, S. Bennington, J. Treadgold, and R. Coleman, Phys. B (Amsterdam) 385–386, 1029 (2006).
- [26] O. Sobolev and J. T. Park, J. Large-Scale Res. Facilities 1, A13 (2015).
- [27] H. M.-L. Zentrum et al., J. Large-Scale Res. Facilities 1, A12 (2015).
- [28] F. Semadeni, B. Roessli, and P. Böni, Phys. B (Amsterdam) 297, 152 (2001), Proceedings of the Third International Workshop on Polarised Neutrons.
- [29] R. I. Bewley, J. Taylor, and S. Bennington, Nucl. Instrum. Methods, Phys. Res. Sect. A 637, 128 (2011).
- [30] S. Toth and B. Lake, J. Phys.: Condens. Matter 27, 166002 (2015).
- [31] S. K. Choi, R. Coldea, A. N. Kolmogorov, T. Lancaster, I. I. Mazin, S. J. Blundell, P. G. Radaelli, Y. Singh, P. Gegenwart, K. R. Choi *et al.*, Phys. Rev. Lett. 108, 127204 (2012).
- [32] S. Blundell, *Physics of Magnetism and Magnetic Materials* (Oxford University Press, UK, 2001).
- [33] A. L. Chernyshev, M. E. Zhitomirsky, N. Martin, and L.-P. Regnault, Phys. Rev. Lett. **109**, 097201 (2012).
- [34] E. S. Klyushina, B. Lake, A. Islam, T. Guidi, and M. Mansson (unpublished).
- [35] K. Yosida, *Theory of Magnetism* (Springer, Germany, 2001).
- [36] G. L. Squires, *Thermal Neutron Scattering* (Dover, New York, 1996).